doi: 10.1093/pasj/xxx000

arXiv:1605.01724v1 [astro-ph.HE] 5 May 2016

Hard X-ray Luminosity Function of Tidal Disruption Events: First Results from *MAXI* Extragalactic Survey

Taiki Kawamuro[1], Yoshihiro Ueda[1], Megumi Shidatsu[2], Takafumi Hori[1], Nobuyuki Kawai[3], Hitoshi Negoro [4], and Tatehiro Mihara [2].

[1]Department of Astronomy, Kyoto University, Kyoto 606-8502, Japan
[2]*MAXI* team, RIKEN, 2-1, Hirosawa, Wako-shi, Saitama 351-0198, Japan
[3]Department of Physics, Faculty of Science Tokyo Institute of Technology, Tokyo 152-8551, Japan
[4]Department of Physics, Nihon University, 1-8-14 Kanda-Surugadai, Chiyoda-ku, Tokyo 101-8308, Japan

*E-mail: kawamuro@kusastro.kyoto-u.ac.jp

Received ; Accepted

Abstract

We derive the first hard X-ray luminosity function (XLF) of stellar tidal disruption events (TDEs) by supermassive black holes (SMBHs), which gives an occurrence rate of TDEs per unit volume as a function of peak luminosity and redshift, utilizing an unbiased sample observed by the Monitor of All-sky X-ray Image (*MAXI*). On the basis of the light curves characterized by a power-law decay with an index of $-5/3$, a systematic search using the *MAXI* data in the first 37 months detected four TDEs, all of which have been found in the literature. To formulate the TDE XLF, we consider the mass function of SMBHs, that of disrupted stars, the specific TDE rate as a function of SMBH mass, and the fraction of TDEs with relativistic jets. We perform an unbinned maximum likelihood fit to the *MAXI* TDE list and check the consistency with the observed TDE rate in the *ROSAT* all sky survey. The results suggest that the intrinsic fraction of the jet-accompanying events is 0.0007–34%. We confirm that at $z \lesssim 1.5$ the contamination by TDEs to the hard X-ray luminosity functions of active galactic nuclei is not significant and hence that their contribution to the growth of SMBHs is negligible at the redshifts.

Key words: galaxies: individuals (*Swift* J1112.2-8238, *Swift* J164449.3+573451, *Swift* J2058.4+0516, NGC 4845) – X-rays: galaxies

1 INTRODUCTION

The nature of supermassive black holes (SMBHs) that reside in inactive galaxy nuclei is very difficult to explore, compared with those of accreting ones observed as active galactic nuclei (AGNs). However, when the orbital path of a star is close enough to a SMBH to be disrupted by the tidal force exceeding the self-gravity of the star, a luminous flare in the UV/X-ray bands is predicted (Rees 1988). This is called a tidal disruption event (TDE). Observations of TDEs are important to take a census of dormant SMBHs and to investigate their environments. Moreover, thanks to their large luminosities, TDEs provide us with valuable opportunities to study distant "inactive" galactic nuclei.

X-ray surveys covering a large sky area are very useful to detect TDEs, because we cannot predict when and where an event occurs. In fact, wide-area X-ray surveys performed with *ROSAT*, *XMM-Newton*, *INTEGRAL*, and *Swift* (e.g., Komossa & Bade 1999; Esquej et al. 2007; Burrows et al. 2011; Saxton

© 2014. Astronomical Society of Japan.

et al. 2012; Nikołajuk & Walter 2013) have discovered many of the TDEs reported so far. Some of TDEs have also been detected in the optical and UV bands (e.g., Gezari et al. 2006, 2008, 2012; Arcavi et al. 2014; Holoien et al. 2014; van Velzen et al. 2011). Since the first detection of a TDE, which occurred in NGC 5905 (Bade et al. 1996), a few tens of X-ray TDEs have been identified (Komossa 2012). The identifications of TDEs were mainly based on their variability characteristics, such as a large amplitude and the unique decline law of the light curve (e.g., Komossa & Bade 1999), which are supported by both analytic solutions (Rees 1988; Phinney 1989) and numerical simulations (e.g., Evans & Kochanek 1989).

The recent hard X-ray survey with *Swift*/BAT and subsequent X-ray observations detected three TDEs accompanied by relativistic jets (Burrows et al. 2011; Cenko et al. 2012; Brown et al. 2015). Presence of the jets was suggested also from follow-up observations in the radio band (Zauderer et al. 2011). In these TDEs, the X-ray fluxes were dominated by non-thermal emission in the beamed jets, unlike in "classical" TDEs, where one observes blackbody radiation emitted from the stellar debris accreted onto the SMBH. Thus, it is interesting to explore what fraction of TDEs produces relativistic jets and what the physical mechanism to launch the jets is.

Theoretically, the occurrence rate of TDEs is estimated to be 10^{-5}–10^{-4} galaxy^{-1} yr^{-1} (e.g., Magorrian & Tremaine 1999), and its dependence on SMBH mass is calculated (e.g., Wang & Merritt 2004; Stone & Metzger 2014). In fact, many observational results (e.g., Donley et al. 2002; Esquej et al. 2008; Maksym et al. 2010) are in rough agreements with the predicted TDE rate. An important quantity that describes the statistical properties of TDEs is the "luminosity function", i.e., the luminosity dependence of the TDE rate. The luminosity function of TDEs is highly useful in evaluating the effect of TDEs on the growth history of SMBHs and in predicting the number of detectable events in future surveys. Considering that the flare luminosity of a TDE depends on the SMBH mass (e.g., Ulmer 1999; Li et al. 2002), it is possible theoretically to estimate the luminosity function of TDEs (Milosavljević et al. 2006). However, observational studies that directly constrain the TDE luminosity function based on a statistically complete sample have been highly limited so far.

In this paper, we derive the hard X-ray luminosity function of TDEs, using a statistically complete sample obtained with the Monitor of All-sky X-ray Image (*MAXI*) mission. For this purpose, we systematically search for hard X-ray transient events at high galactic latitudes ($|b| > 10^\circ$), and identify TDEs. We then derive the luminosity functions of TDEs associated with and without relativistic jets individually. This result also enables us to estimate the contribution of TDEs to the growth of SMBHs.

This paper is organized as follows. Section 2.1 presents the overview of the *MAXI* observations. In Section 2.3, the light-curve analysis of the *MAXI* sources to identify TDEs is presented. The derivation of the X-ray luminosity function of TDEs is described in Section 3. Section 4 gives discussion based on our XLF model, including the contribution of TDEs to the XLF of AGNs and to the evolution of the SMBH mass density. Section 5 presents the summary of our work. Appendix A describes the method of detecting transient sources from the *MAXI* data. Throughout this paper, we assume a Λ cold dark-matter model with $H_0 = 70$ km s^{-1} Mpc^{-1}, $\Omega_{\rm M} = 0.3$, and $\Omega_\Lambda = 0.7$. The "log" denotes the base-10 logarithm, while the "ln", the natural logarithm.

2 Search of TDE From *MAXI* Data

2.1 Observations and Data Reduction

The *MAXI* mission (Matsuoka et al. 2009) on the International Space Station (ISS) has been monitoring all sky in the X-ray band since 2009. *MAXI* achieves the highest sensitivity as an all-sky monitor, and is highly useful to detect X-ray transient events, including TDEs. It carries two types of cameras, the Gas Slit Cameras (GSCs; Mihara et al. 2011), consisting of 12 counters, and the Solid-state Slit Camera (Tomida et al. 2011). In this paper, we only utilize the data of the GSCs, which covers the energy band of 2–30 keV. The GSCs have two instantaneous fields-of-view of $1^\circ.5 \times 160^\circ$ separated by 90 degrees. They rotate with a period of 92 minutes according to the orbital motion of the ISS, and eventually covers a large fraction of the sky (95%) in one day (Sugizaki et al. 2011).

To search the *MAXI*/GSC data for transient events, we analyze those taken in the first 37 months since the beginning of the operation (from 2009 September 23 to 2012 October 15). We also restrict our analysis to high galactic latitudes ($|b| > 10^\circ$). Exactly the same data were analyzed to produce the second *MAXI*/GSC catalog (Hiroi et al. 2013), which contains 500 sources detected in the 4–10 keV band from the data integrated over the whole period. The details of the data selection criteria are described in Section 2 of Hiroi et al. (2013).

2.2 Identification of TDEs in *MAXI* Catalogs

TDEs are transient events that become bright for a typical time scale of months to years (e.g., Komossa & Bade 1999). Hence, they may be missed with the *MAXI* Alert System (Negoro et al. 2012), which is currently optimized to detect variability of sources on time scales from hours to a few days. Also, faint TDEs may not be detected in the 2nd *MAXI* catalog (Hiroi et al. 2013), because the long integration time of 37 months works to smear the signals, making the time averaged significance lower than the threshold.

To detect such transient events as completely as possible,

we newly construct the *MAXI*/GSC "*transient source catalog*" based on the same data as used by Hiroi et al. (2013). The analysis is optimized to find variable objects on the time scale of 30 or 90 days. Namely, we split the whole data into 30 or 90 day bins, and independently perform source detection from each dataset to search for new sources that are not listed in the 2nd *MAXI* catalog (Hiroi et al. 2013). As a result, we detect 10 transient sources with the detection significance $s_{\rm D} > 5.5$ in either of the time-sliced datasets, where $s_{\rm D}$ is defined as (best-fit flux in 4-10 keV) / (its 1σ statistical error). The details of the analysis procedure and the resultant light curves of the transient sources are given in Appendix A. As an example, Figure 1 shows the *MAXI*/GSC significance map around *Swift* J164449.3+573451 (hereafter *Swift* J1644+57), a transient source detected by this method. This object is significantly detected in the data of 30 days during the outburst (left panel), while it is not in the 37-month data (right panel). We estimate the sensitivity limit for the peak flux averaged for 30 days is ~ 2.5 mCrab.

On the basis of positional coincidence, we identify 3 TDE candidates in the *MAXI* transient source catalog from the literature, *Swift* J1112.2-8238 (hereafter *Swift* J1112-82; Brown et al. 2015), *Swift* J1644+57 (Burrows et al. 2011), and *Swift* J2058.4+0516 (hereafter *Swift* J2058+05; Cenko et al. 2012). They are located at $z = 0.89$, $z = 0.354$, and $z = 1.1853$, and the (isotropic) luminosities in the 4–10 keV band are estimated to be $10^{47.1}$ erg s^{-1}, $10^{46.6}$ erg s^{-1}, and $10^{47.5}$ erg s^{-1}, respectively. We also identify another candidate that occurred in NGC 4845 (Nikołajuk & Walter 2013), which has been already listed in the 2nd *MAXI*/GSC catalog (Hiroi et al. 2013). The 30-day averaged peak flux in the 4–10 keV band is 3.2 mCrab, with a significance of $s_{\rm D} = 6.8$, which corresponds to a luminosity of $10^{42.3}$ erg s^{-1} at $z = 0.004110$. We note, however, that the X-ray flare of NGC 4845 may be attributed to a variable AGN, which is supported by the radio observation of the unresolved central core (Irwin et al. 2015). From the time evolution of the radio spectrum, Irwin et al. (2015) also suggested the presence of an expanding outflow or a jet, which may be associated with the X-ray flare. It is not yet unclear whether the X-ray flare is due to a TDE or the AGN. The detailed information of each TDE from the literature (Burrows et al. 2011; Cenko et al. 2012; Nikołajuk & Walter 2013; Zauderer et al. 2013; Brown et al. 2015; Pasham et al. 2015) is summarized in Table 1.

2.3 Search for Unidentified TDEs

To constrain statistical properties of TDEs, such as the occurrence rate as a function of X-ray luminosity (i.e., X-ray luminosity function = XLF hereafter), it is very important to perform their complete survey at a given flux limit. Hence, we search for other possible TDEs that are not reported in the literature from these *MAXI* catalogs. We make use of the general characteristics of the light curve pattern of TDEs. As mentioned in Section 1, a TDE shows a rapid flux increase followed by a power-law decay with an index of -5/3 as a function of time (Rees 1988; Phinney 1989).

For this purpose, we make the light curves of all sources in the 2nd *MAXI*/GSC catalog (Hiroi et al. 2013) and in the transient catalog (Appendix A) in 10 days, 30 days, and 90 days bins, in three energy bands, 3–4 keV, 4–10 keV, and 3–10 keV. The fluxes in each time bin are obtained by the same image fitting method as described in Appendix A by fixing the source positions. We discard the data when the photon statistics is too poor within each bin (see subsection 2.1 in Isobe et al. (2015) for details). Using the light curve of Crab nebula analyzed in the same way, we estimate a systematic uncertainty in the flux is $\sim$10%, which is added to the statistical error.

As the reference, we analyze the light-curve pattern of the four identified TDEs, *Swift* J1112-82, *Swift* J1644+57, *Swift* J2058+05, and NGC 4845. We find that all of them show the following two characteristics. The first one is high variability amplitudes; the ratio between the highest flux and the one of the previous bin in the 30-day (90-day) averaged light curves is 7.0 (1.6), 16.3 (7.7), 8.2 (2.4), and 1.4 (6.8) for *Swift* J1112-82, *Swift* J1644+57, *Swift* J2058+05, and NGC 4845, respectively. Here, we assign a flux of 5×10^{-12} erg s^{-1} cm^{-2} (4–10 keV) for each bin when the source is undetected, which is the sensitivity limit of the 2nd *MAXI* catalog (Hiroi et al. 2013). The second characteristic is that the decay light curves are consistent with a power-law profile of $t^{-5/3}$, where t is time since the onset time of each TDE. We note that the time of the flux peak, $t_{\rm p}$, is delayed from the TDE onset time by approximately 80 days for NGC 4845, 20 days for *Swift* J1644+57 and *Swift* J2058+05, and 5 days for *Swift* J1112-82. Hence, we set the central day of the bin showing the highest flux as $t_{\rm p}$, and estimate the TDE onset time by correcting for these offsets. We confirm that the 10-days light curves in the 3–10 keV band follow power-law profiles, as shown in Figure 2. A power-law fit to the light curve over 90 days after the peak flux is found to be acceptable in terms of a χ^2 test, yielding the best-fit index of $-1.86^{+0.45}_{-1.55}$, $-1.94^{+0.39}_{-0.48}$, $-1.92^{+0.58}_{-0.73}$, and $-2.00^{+1.14}_{-1.25}$ for *Swift* J1112-82, *Swift* J1644+57, *Swift* J2058+05, and NGC 4845, respectively. The errors denote statistical ones at 90% confidence limits, and they are all consistent with $-5/3$. Accordingly, we apply the above two conditions to the light curves of all *MAXI* sources (in total 506) except for the four TDEs. First, we find 12 (12) objects satisfy the criterion that the ratio between the highest and second highest flux bins is larger than 5 in the 30 (90) day light curve. For these candidates, we then perform the same light-curve fitting with a power-law profile as described above. The time delay from the TDE onset to the observed flux peak is set to be either 5 days, 20 days, or 80 days. As a result, we find that none of them show a decaying index consistent

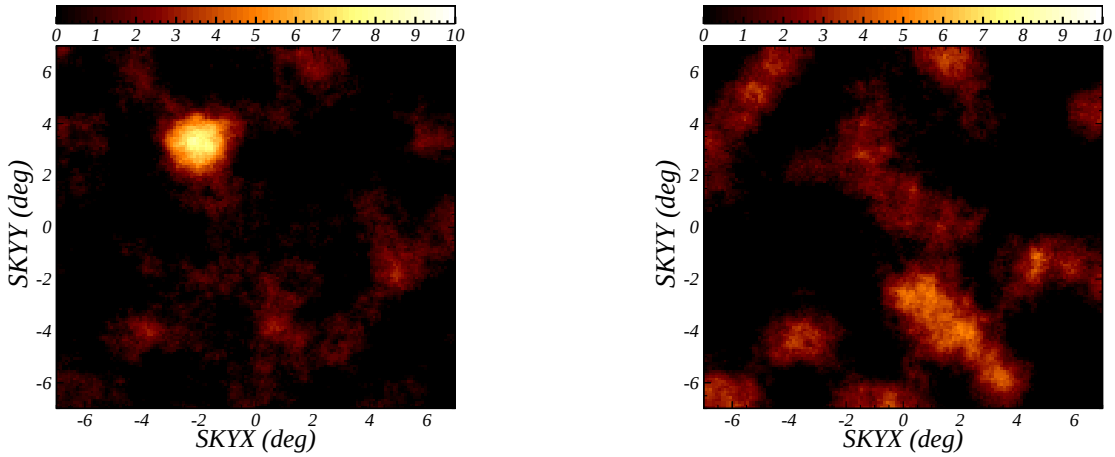

Fig. 1. (Left) Significant map around *Swift* J1644+58 (left upper source) obtained from the data integrated for 30 days when the object was the brightest. (Right) The same but obtained from the total 37-month data.

Table 1. Our Sample of Tidal Disruption Events

Name	z	$\log L_{4-10\mathrm{keV}}$	Γ	δ	M_*
[1]	[2]	[3]	[4]	[5]	[6]
Swift J1112.2-8238	0.89	47.1	-	-	-
Swift J164449.3+573451	0.354	46.6	10	16	0.15
Swift J2058.4+0516	1.1853	47.5	> 2	-	0.1
NGC 4845	0.004110	42.3	-	-	0.02

Notes.
Col. [1]: Name of the TDE.
Col. [2]: Redshift.
Col. [3]: Luminosity (erg s^{-1}) in the 4–10 keV band.
Col. [4]: The Bulk Lorentz factor.
Col. [5]: The Doppler factor.
Col. [6]: Accreted mass in units of solar mass.

with $-5/3$ except for the objects identified as AGNs or X-ray galactic sources. Thus, we conclude that *MAXI* detected only the four TDEs identified above during the first 37 months of its operation, which can be regarded as a statistically complete sample at the sensitivity limit of *MAXI* for transient events, *as long as TDEs share similar characteristics in the X-ray light curve to those of the known events.* According to numerical simulations, the index of the power-law decay becomes steeper than $-5/3$ when the star is not fully disrupted (Guillochon & Ramirez-Ruiz 2013). Such events would be missed in our sample. We find that four TDE candidates reported by Hryniewicz & Walter (2016) from the *Swift*/BAT ultra-hard X-ray band (20–195 keV) data were not significantly detected in the *MAXI* data covering the same epoch. The details are given in Appendix B. In all events, the flux upper limit in the *MAXI* band is smaller by a factor of $\sim$4 than that expected from the Swift/BAT flux by assuming a photon index of 2.0. This implies that these TDE candidates might have unexpectedly hard spectra or be subject to heavy obscuration. Such TDEs, if any, are not considered in our analysis.

The continuous monitoring data of *MAXI* provide us with unique information on the X-ray light curve of TDEs in the 3–10 keV band, which can be compared with those obtained with *Swift*/BAT in the 14–195 keV band. Figure 3 plots the *MAXI* light curves in 1-day bins of the three TDEs except for NGC 4845, which was too faint to be examined on shorter time scales than 10 days. We find that the luminosity peaked at MJD = 55729, MJD = 55649, and MJD = 55701 for *Swift* J1112–82, *Swift* J2058+05, and *Swift* J1644+57, respectively, which are all consistent with those determined with *Swift*/BAT within 1 day (Burrows et al. 2011; Cenko et al. 2012; Brown et al. 2015). Thus, there is no evidence for significant (> 1 day) time lags between the soft (< 10 keV) and hard (> 10 keV) bands.

3 Hard X-ray Luminosity Function of Tidal Disruption Events

3.1 Definition of Luminosities

In this section, we summarize the definitions of TDE luminosities used in our analysis ($L^{\mathrm{obs}}_{\mathrm{X,ins}}(t)$, $L^{\mathrm{obs}}_{\mathrm{X}}$, and L_{x}). To make

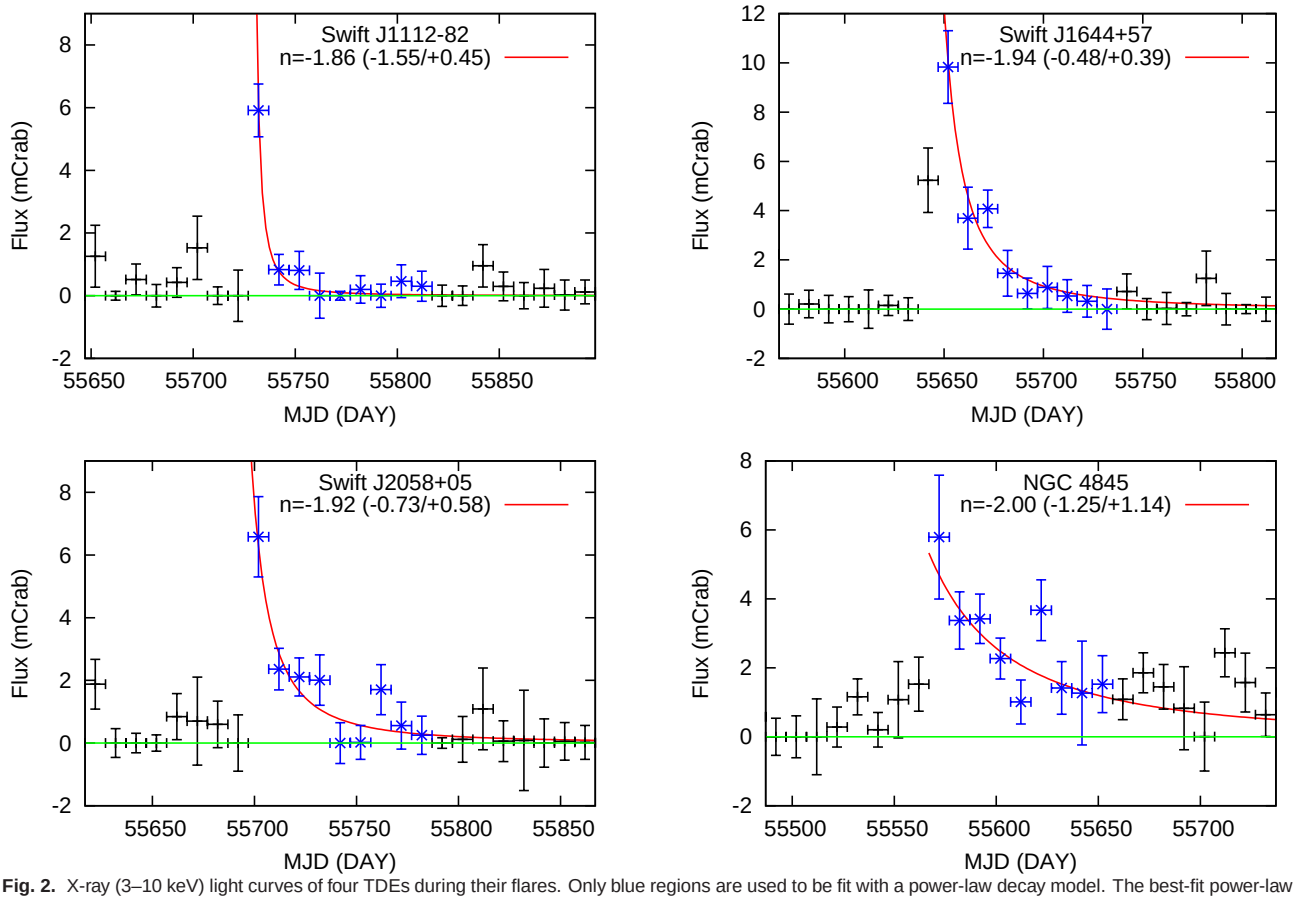

Fig. 2. X-ray (3–10 keV) light curves of four TDEs during their flares. Only blue regions are used to be fit with a power-law decay model. The best-fit power-law index (n) is indicated in each panel with errors at 90% confidence level.

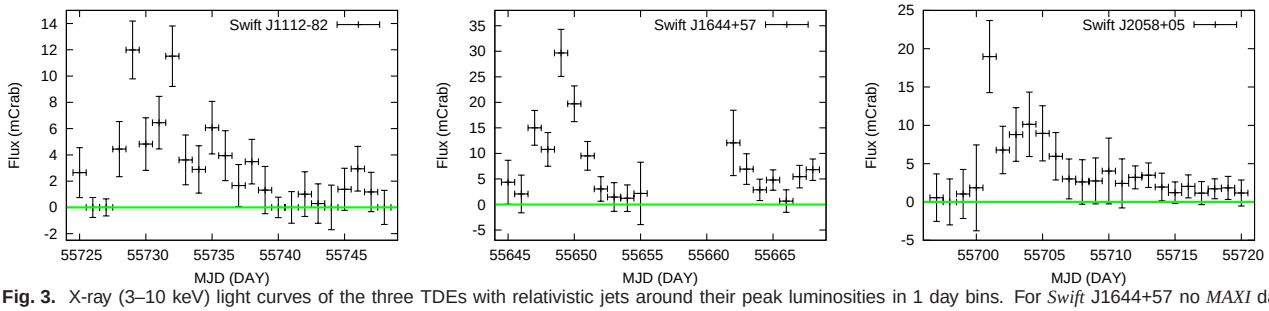

Fig. 3. X-ray (3–10 keV) light curves of the three TDEs with relativistic jets around their peak luminosities in 1 day bins. For *Swift* J1644+57 no *MAXI* data were obtained around MJD ∼55660.

luminosity conversion between different energy bands, we need to assume model spectra of TDEs. According to the previous studies on TDEs observed in the X-ray band (e.g., Esquej et al. 2007; Burrows et al. 2011; Nikołajuk & Walter 2013), we can approximate that the X-ray spectra of TDEs without jets are composed of blackbody radiation and a power law, which originate from the optically thick disk and its Comptonized component by hot corona, respectively. For TDEs with jets, a relativistically beamed power law is added to the above spectrum. A representative spectrum is shown in Figure 4, where the photon indices of the two power-law components are assumed to be 2. Modelling the decay profile of the lightcurve of a TDE with $(t/t_{\rm p})^{-5/3}$, we can relate an observed, instantaneous luminosity at t in a given energy band calculated by assuming isotropic emission, $L^{\rm obs}_{\rm X,ins}(t)$, to its corresponding peak luminosity $L^{\rm obs}_{\rm X}$, as

$$L^{\rm obs}_{\rm X,ins}(t) = L^{\rm obs}_{\rm X}\left(\frac{t}{t_{\rm p}}\right)^{-5/3} (t \geq t_{\rm p}). \quad (1)$$

We define $L_{\rm x}$ as the "intrinsic" peak luminosity of the Comptonized power-law component in the rest-frame 4–10 keV band. It can be converted into the "observed" peak luminosity by

$$L^{\rm obs}_{\rm X} = CL_{\rm X}, \quad (2)$$

where C (C_0 or C_1; see below) is the conversion factor that depends on the shape of the spectrum, redshift, and viewing angle with respect to the jet axis (for TDEs with jets).

Introducing the fraction of TDEs with jets in total TDEs, $f_{\rm jet}$, we divide TDEs into two types, one with jets and the other without jets. For the TDEs without jets, whose fraction is $(1-f_{\rm jet})$, the conversion factor C_0 can be written as

$$C_0 = \omega_{\rm pow} + \omega_{\rm bb}, \tag{3}$$

where $\omega_{\rm pow}$ and $\omega_{\rm bb}$ are those for the Comptonized (power-law) and blackbody components, respectively. We normalize $\omega_{\rm pow}$ to unity when $L_{\rm X}^{\rm obs}$ of a TDE at $z=0$ is defined in the 4–10 keV band and its spectrum is not absorbed. The factor $\omega_{\rm bb}$ depends on the broadband spectrum of a TDE, as detailed in the third paragraph of Section 3.6. Note that the blackbody component is negligible in the 4–10 keV band because its temperature is expected to be much lower than a few keV (Section 3.6).

For TDEs with relativistic jets, the conversion factor C_1 can be written as

$$C_1 = \omega_{\rm pow} + \omega_{\rm bb} + \omega_{\rm jet}\eta_{\rm jet}\delta^4 \tag{4}$$

where the last term represents the jet contribution. Here, $\omega_{\rm jet}$ takes account of the energy-band conversion, $\eta_{\rm jet}$ is the fraction of the intrinsic luminosity (i.e., that would be observed without beaming) of the jet in $L_{\rm x}$ (the peak luminosity of the Comptonized component), and δ is the Doppler factor. It is represented as

$$\delta = \frac{1}{\Gamma - \sqrt{\Gamma^2-1}\cos\theta}, \tag{5}$$

where Γ is the Lorentz factor and θ is the viewing angle with respect to the jet axis. The observed luminosity from the jet becomes larger than the intrinsic one by a factor of δ^4 with a frequency shift by δ. In our analysis, we adopt $\Gamma = 10$, which is suggested from the analysis of the spectrum energy distribution of *Swift* J1644+57 by Burrows et al. (2011). Then, θ can be estimated if δ is constrained from the observations, as listed in Table 1 for *Swift* J1644+57. We also adopt $\eta_{\rm jet} = 0.1$ as a standard value. It is confirmed that our main results do not sensitively depend on the choice of Γ or $\eta_{\rm jet}$ (see Section 3.7). Throughout our analysis, we do not take into account possible precession of the jets due to the Lense-Thirring effect, as predicted by Stone & Loeb (2012). This effect would be negligible because our calculation of the XLF is based on the flux averaged over 30 days, which smears out the effect. The conversion factors C_0 and C_1 are dimensionless, composed only of the dimensionless factors (ω, $f_{\rm jet}$, and δ).

3.2 TDE Sample

We regard that the four identified TDEs listed in Table 1 constitute a complete sample from the *MAXI* survey for 37 months, and we utilize them to derive the XLF. When integrated for 30 days, the *MAXI* survey covers all the high Galactic latitudes ($|b| > 10^\circ$) region, which corresponds to 83% of the entire sky. As described in the previous section, we have searched for TDEs based on 30 days or 90 days binned light curves.

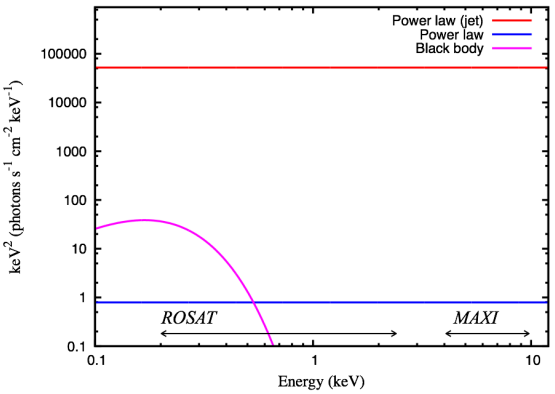

Fig. 4. A representative spectrum of a TDE with $T_{\rm bb} = 5\times10^5$ K. The three components are shown (red: jet component with $\delta = 16$, blue: Comptonized component, magenta: blackbody component). The unit of the vertical axis is arbitrary.

Thus, the sensitivity limit for the 30-days averaged peak flux of TDEs to which our survey is complete is determined by that for 30-days integrated data of *MAXI*/GSC, which is 2.5 mCrab, or 3×10^{-11} erg s^{-1} cm^{-2} (4–10 keV). For simplicity, we ignore the dependence of the sensitivity on sky positions (Hiroi et al. 2013), whose effects are much smaller than the statistical uncertainties in the XLF parameters.

It is necessary to assume a spectrum to derive the luminosity from the observed count rate of *MAXI*/GSC. Because the blackbody component can be ignored in the 4–10 keV band, here we assume a power-law spectrum absorbed with the hydrogen column-densities reported by the previous studies (Burrows et al. 2011; Cenko et al. 2012; Nikołajuk & Walter 2013; Brown et al. 2015). In the following analysis, for simplicity, we always adopt a photon index of 2 both for the Comptonization and jet components, as a representative value. In fact, for all four TDEs, the hardness ratio defined as $(H-S)/(H+S)$, where H and S is the count rates obtained from the *MAXI* data in the 4–10 keV and 3–4 keV bands, respectively, is consistent with a photon index of 2.0 within uncertainties. In this case, the K-correction factor is always unity and $\omega_{\rm pow} = \omega_{\rm jet}$. The calculated peak luminosity of each TDE is listed in Table 1. Its systematic error due to the uncertainty in the peak-flux time within the bin size of the *MAXI* light curve has negligible effect on our conclusions.

3.3 Formulation of TDE X-ray Luminosity Function

We define the XLF of TDEs so that $\mathrm{d}\Phi(L_{\rm x},z)/\mathrm{d}L_{\rm x}$ represents the TDE occurrence rate per unit co-moving volume per $L_{\rm x}$ per unit rest-frame time, as a function of $L_{\rm x}$ and z, in units of Mpc^{-3} $L_{\rm x}^{-1}$ yr^{-1}. Note that this function has an additional dimension of per unit time compared with the "instantaneous" XLF of TDEs and the XLF of AGNs (see subsection 4.3), which represents the number density of TDEs and AGNs, respectively,

observed in a single epoch.

In our work, we make simple assumptions for modelling the shape of the TDE XLF. First, we write the TDE occurrence rate per unit volume as a function of SMBH mass. It should be proportional to the product of the SMBH mass function (i.e., comoving number density of SMBHs) and a specific TDE rate in a single SMBH. The local SMBH mass function can be derived from the local luminosity function of galaxies by using the Faber-Jackson relation between the galaxy luminosity and the SMBH mass, $L_{\rm gal} \propto M_{\rm BH}^k$ (e.g., Ferrarese 2002; Milosavljević et al. 2006). It has a form of the Schechter function represented as

$$\psi(M_{\rm BH*}; M_{\rm BH}){\rm d}M_{\rm BH} = \psi_0 \left(\frac{M_{\rm BH}}{M_{\rm BH*}}\right)^{\gamma} e^{-(\frac{M_{\rm BH}}{M_{\rm BH*}})^k} \frac{{\rm d}M_{\rm BH}}{M_{\rm BH*}}. \quad (6)$$

Here, $\gamma = k(\alpha+1)-1$, where α is a parameter of the galaxy luminosity function defined as $\Psi(L_{\rm gal*}; L_{\rm gal}){\rm d}L = \Psi_0 (L_{\rm gal}/L_{\rm gal*})^{\alpha} e^{-L_{\rm gal}/L_{\rm gal*}} {\rm d}L_{\rm gal}/L_{\rm gal*}$. The subscript $*$ indicates the characteristic parameter. Unless otherwise noted, we adopt $k = 0.8$, $\Psi_0 = 0.007$, $\log(M_{\rm BH*}/M_\odot) = 8.4$, and $\alpha = -1.3$ according to the results obtained by Marconi & Hunt (2003) and Blanton et al. (2001), where $M_\odot$ is the solar mass. We refer to the dependence of the specific TDE rate on SMBH mass derived by Stone & Metzger (2014),

$$\xi \propto M_{\rm BH}^{\lambda}, \quad (7)$$

where λ is chosen to be -0.4.

To represent the TDE occurrence rate as a function of *luminosity*, we further make an assumption that the peak luminosity L of a TDE (i.e., that free from the jet luminosity) is proportional to the SMBH mass, or equivalently, a constant fraction of the Eddington luminosity, $\lambda_{\rm Edd}$. Then, by converting $M_{\rm BH}$ into L in the product of $\psi(M_{\rm BH*}; M_{\rm BH})$ and ξ, we can express the occurrence rate of TDEs per unit volume in terms of L as

$$\phi(L_*; L){\rm d}L = \psi_0 \xi_0 \left(\frac{L}{L_*}\right)^{\gamma+\lambda} e^{-(\frac{L}{L_*})^k} \frac{{\rm d}L}{L_*}. \quad (8)$$

We incorporate a redshift dependence of the TDE XLF with an evolution factor of $(1+z)^p$ that is multiplied to the local XLF. Thus, the TDE XLF is formulated as

$$\frac{{\rm d}\Phi(L_{\rm x}, z)}{{\rm d}L_{\rm x}} {\rm d}L_{\rm x} = (1+z)^p \phi(L_{\rm x*}; L_{\rm x}){\rm d}L_{\rm x}. \quad (9)$$

3.4 Mass Function of Stars Disrupted by SMBHs

A TDE occurs only when the tidal disruption radius, $R_{\rm TDE} = R_*(M_{\rm BH}/M_*)^{1/3}$, where M_* and R_* are the mass and radius of the star, is larger than the Schwarzschild radius, $R_{\rm Sch}$ ($\equiv 2GM_{\rm BH}/c^2$, where G is the gravitational constant.). For a given star, there is an upper boundary for the mass of a SMBH that can cause a TDE. Hence, the mass function of stars should be incorporated in calculating the actual TDE XLF. We approximate it by the shape of an initial mass function (IMF) with an upper star mass boundary $M_{*,\rm max}$, considering that very massive stars are already dead due to their short life time. Here we employ the IMF derived by Kroupa (2001), which utilizes a larger sample than that by Salpeter (1955) and is similar to that by Chabrier (2003). The normalized stellar mass function is continuously composed of next three equations;

$$P(M_*){\rm d}\log M_* \propto$$
$$M_*^{0.7} (M_{*,\rm min} \le M_* < 0.08 M_\odot) \quad (10)$$
$$M_*^{-0.3} (0.08 M_\odot \le M_* < 0.5 M_\odot) \quad (11)$$
$$M_*^{-1.3} (0.5 M_\odot \le M_* \le M_{*,\rm max}), \quad (12)$$

and satisfies

$$\int_{M_{*,\rm min}}^{M_{*,\rm max}} P(M_*){\rm d}\log M_* = 1, \quad (13)$$

where we set $M_{*,\rm min} = 0.01 M_\odot$ and $M_{*,\rm max} = 1.0 M_\odot$. We confirm that the choice of $M_{*,\rm max}$ does not significantly affect our conclusions (Section 3.7).

3.5 Maximum Likelihood Fit

We adopt the unbinned maximum likelihood (ML) method to constrain the XLF parameters. While the ML fit gives the best-fit parameters, the goodness of the fit cannot be evaluated. Hence, we perform one dimensional Kolmogorov-Smirnov test (hereafter KS test; e.g., Press et al. 1992) separately for the redshift distribution and for the luminosity distribution between the observed data and best-fit model. The p-value, the chance of getting observed data set, is evaluated from the D-value assuming the one-sided KS test statistic. The D-value is chosen to be the maximum value among the absolute distances between an empirical cumulative distribution function and a theoretical one.

We define the likelihood function as

$$\mathcal{L} = -2 \sum_i \ln \frac{\int\int\int N(L_{\rm x}, L_{{\rm x}i}^{\rm obs}, z_i, M_*, \theta){\rm d}L_{\rm x}{\rm d}\log M_* {\rm d}\Omega/2\pi}{\int\int\int\int\int N(L_{\rm x}, L_{\rm x}^{\rm obs}, z, M_*, \theta){\rm d}L_{\rm x}{\rm d}L_{\rm x}^{\rm obs}{\rm d}z{\rm d}\log M_* {\rm d}\Omega/2\pi}, \quad (14)$$

where the subscript index i refers to each TDE and the term $N(L_{\rm x}, L_{\rm x}^{\rm obs}, z, M_*, \theta){\rm d}L_{\rm x}{\rm d}L_{\rm x}^{\rm obs}{\rm d}z{\rm d}\log M_* {\rm d}\Omega/2\pi$ represents the differential number of observable TDEs with the intrinsic peak luminosity $L_{\rm x}$, the observed one $L_{\rm x}^{\rm obs}$, the redshift z, the mass of the star M_*, and the viewing angle θ, expected from the survey (note that θ is related to the solid angle as ${\rm d}\Omega = 2\pi {\rm d}(\cos(\theta))$). By considering that the fraction of TDEs with jets among all TDEs is $f_{\rm jet}$, the differential number is calculated as

$$N(L_{\rm x}, L_{\rm x}^{\rm obs}, z, \theta, M_*) = \left\{(1-f_{\rm jet})\delta_{\rm D}(C_0 L_{\rm x} - L_{\rm x}^{\rm obs}) + f_{\rm jet}\delta_{\rm D}\left(C_1 L_{\rm x} - L_{\rm x}^{\rm obs}\right)\right\} \times \frac{{\rm d}\Phi(L_{\rm x}, z)}{{\rm d}L_{\rm x}} \frac{d_{\rm L}^2(z)}{1+z} c \frac{{\rm d}\tau}{{\rm d}z} A\left(\frac{L_{\rm x}^{\rm obs}}{d_{\rm L}^2}\right) \frac{\Delta T}{1+z} P(M_*), \quad (15)$$

where $\delta_{\rm D}(x)$ is the Dirac δ-function, $d_{\rm L}$ the luminosity distance, c the light velocity, ${\rm d}\tau/{\rm d}z$ the differential look-back time, A the survey area at the flux limit of $L_{\rm x}^{\rm obs}/4\pi d_{\rm L}^2$, and ΔT ($=37$ months) the survey time at the observer's frame. The factor $1/(1+z)$ comes from the time dilation at z.

Since our sample size of TDEs is very small (four), we fix the following parameters of the XLF model, which cannot be well constrained from the data. We adopt the characteristic luminosity of $\log L_{\rm x*}=44.6$ corresponding to the Eddington ratio of $\lambda_{\rm Edd}=1$ (see next paragraph). As mentioned previously and listed in Table 2, the Lorentz factor of the jets, the dependence of the specific TDE rate on SMBH mass, the fraction of the intrinsic jet luminosity in $L_{\rm x}$, and the upper mass boundary of tidally disrupted stars are fixed at $\Gamma=10$, $\lambda=-0.4$, $\eta_{\rm jet}=0.1$, and $M_{*,\rm max}=1.0M_\odot$ as the standard parameters, respectively. Effects on the main results by changing these numbers ($\lambda_{\rm Edd}$, Γ, λ, $\eta_{\rm jet}$, and $M_{*,\rm max}$) from the default values will be examined in Section 3.6 and 3.7. The index of the redshift evolution is assumed to be either $p=0$ (no evolution case) or 4 (strong evolution case). According to the prediction of numerical simulations that the occurrence rate of TDEs increases with the star-formation rate (Aharon et al. 2015), the latter case simply assumes that the TDE rate is proportional to the star-formation rate density, which evolves with $\propto(1+z)^4$ (Pérez-González et al. 2005). Eventually, only $\phi_0\xi_0$ and $f_{\rm jet}$ are left as free parameters.

The minimization procedure is carried out by using the MINUIT software package. We calculate the likelihood function over a redshift range of $z=0$–1.5. The luminosity range is derived from the SMBH range of $\log(M_{\rm BH}/M_\odot)=4$–$8$ for a given $\lambda_{\rm Edd}$ (1.0). To convert the mass into the X-ray luminosity $L_{\rm x}$, we consider a spectra composing of the three components described in Section 3.1 (the blackbody, Comptonization, and jet components). Specifically, we first determine the ratio of the Comptonized component in the 2–10 keV band to the bolometric luminosity without the jet component. Assuming that accretion physics in TDEs is similar to that of AGNs, we refer to the results by Vasudevan & Fabian (2007), who derived the bolometric correction factor (k_{2-10}) from the 2–10 keV band to be $\sim$50 for $\lambda_{\rm Edd}=1.0$. We then convert the luminosity in the 2–10 keV band to that in the 4–10 keV band by assuming a power-law photon index of 2.0. As a result, $\log L_{\rm x}$ spans a range from 40.2 to 44.2 for $\lambda_{\rm Edd}=1.0$. The rest of the bolometric luminosity is attributed to the blackbody emission. The integration range of M_* is determined to satisfy the criterion $R_{\rm TDE}/R_{\rm Sch}\geq 1$. To calculate the tidal disruption radius $R_{\rm TDE}=R_*(M_{\rm BH}/M_*)^{1/3}$, we convert the radius of a disrupted star R_* to a mass M_* with $R_*/R_\odot=(M_*/M_\odot)^{0.8}$ (e.g., Kippenhahn & Weigert 1990). Hence, $R_{\rm TDE}/R_{\rm Sch}$ is a function of M_* and $M_{\rm BH}$, or that of M_*, $\lambda_{\rm Edd}$, and $L_{\rm x}$.

Table 3 summarizes the results of the ML fit for the cosmological evolution index of $p=0$ and $p=4$. The other fixed parameters are also listed in Table 2. One-dimensional KS tests for the distribution of z and for that of $L_{\rm x}^{\rm obs}$ do not rule out both results at the 90% confidence level. The 90% confidence upper and lower limits on $f_{\rm jet}$ are derived, corresponding to the case where the $\mathcal{L}$-value is increased by 2.7 from its minimum. Since the ML method cannot directly determine the normalization ($\psi_0\xi_0$) of the luminosity function, we calculate it so that the predicted number from the model equals to the detected number of the TDEs. The attached error corresponds to the Poisson error in the observed number at the 90% confidence level based on equations (9) and (12) in Gehrels (1986).

Figure 5 displays the results of the TDE XLF as a function of $L_{\rm x}^{\rm obs}$ (observed peak luminosity in the 4–10 keV band), obtained for the cases of $p=0$ and 4. The solid curves plot the best-fit model at $z=0.75$, which is obtained by integrating ${\rm d}\Phi(L_{\rm x},z=0.75)/{\rm d}L_{\rm x}$ over the half solid angle with respect to the jet direction, the mass of disrupted stars, and $L_{\rm x}$ (intrinsic peak luminosity of the Comptonized component) as

$$\begin{aligned}&\Pi(\log L_{\rm x}^{\rm obs},z=0.75)\\ &\quad=\ln(10)\ L_{\rm x}^{\rm obs}\int\int\int {\rm d}L_{\rm x}{\rm d}\log M_*\frac{{\rm d}\Omega}{2\pi}\\ &\quad\times\left\{(1-f_{\rm jet})\delta_{\rm D}(C_0L_{\rm x}-L_{\rm x}^{\rm obs})+f_{\rm jet}\delta_{\rm D}\left(C_1L_{\rm x}-L_{\rm x}^{\rm obs}\right)\right\}\\ &\quad\times\frac{{\rm d}\Phi(L_{\rm x},z=0.75)}{{\rm d}L_{\rm x}}P(M_*).\end{aligned}\tag{16}$$

The data points are plotted by the "$N^{\rm obj}/N^{\rm model}$" method (Miyaji et al. 2001); they are calculated as

$$\Pi(\log L_{\rm x}^{\rm obs},z=0.75)\times\frac{N^{\rm data}}{N^{\rm model}},\tag{17}$$

Table 2. Default Setting of Fixed Parameters

$\lambda_{\rm Edd}$	Γ	λ	$\eta_{\rm jet}$	$M_{*,\rm max}$
[1]	[2]	[3]	[4]	[5]
1.0	10	-0.4	0.1	1.0

Notes.
Col. [1]: Eddington ratio.
Col. [2]: The Lorentz factor.
Col. [3]: Index for the $M_{\rm BH}$ dependence of the TDE rate.
Col. [4]: Fraction of the intrinsic luminosity of the jet in $L_{\rm x}$.
Col. [5]: Upper mass boundary of disrupted stars in units of solar mass.

Table 3. Best-fit parameters

p	$f_{\rm jet}$	$\psi_0\xi_0$	p-value ($L_{\rm x}^{\rm obs}$-dist/z-dist)
[1]	[2]	[3]	[4]
0	$0.012^{+0.122}_{-0.010}$	$1.7^{+1.6}_{-0.9}$	0.16/0.14
4	$0.003^{+0.027}_{-0.002}$	$1.6^{+1.6}_{-0.9}$	0.60/0.40

Notes.
Col. [1]: Index of the redshift evolution.
Col. [2]: Fraction of the TDEs with jets.
Col. [3]: Normalization factor of XLF in units of 10^{-8} Mpc^{-3} $\log L_{\rm x}^{-1}$ yr^{-1}.
Col. [4]: p-value on the basis of the KS-test for each parameter of $L_{\rm x}^{\rm obs}$ and z.

where $N^{\rm data}$ is the number of observed events in each luminosity bin and $N^{\rm model}$ is that predicted by a model. The error bars reflect the 90% confidence level in $N^{\rm data}$ based on the formula of Gehrels (1986). If no event is detected, we plot the 90% upper limit by setting $N^{\rm data} = 2.3$ (Gehrels 1986).

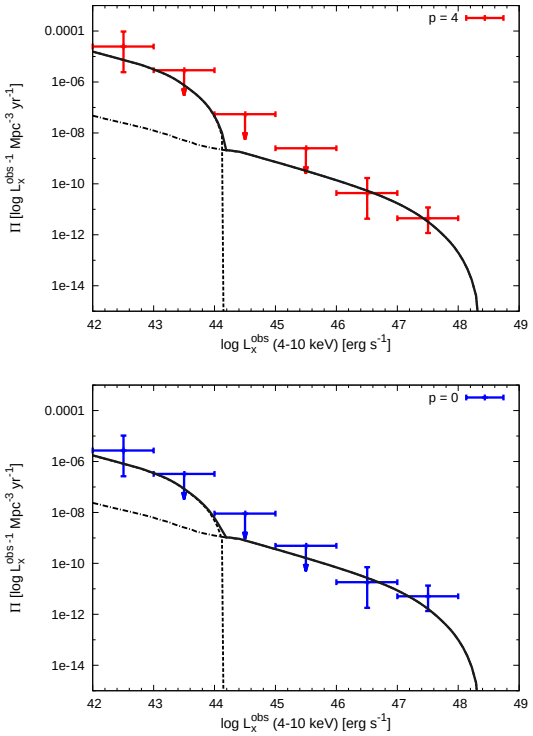

Fig. 5. The best-fit XLF as a function of "observed" peak luminosity at $z = 0.75$ for two evolution indices (left figure: $p = 4$, right figure: $p = 0$). The solid lines represent the total XLF consisting of that of TDEs without jets (dotted line) and that of TDEs with jets (dot-dashed line).

Table 4 lists the TDE occurrence rates per unit volume ($\rm Mpc^{-3}\ yr^{-1}$) in different luminosity ranges predicted from our best-fit TDE XLFs. The attached errors are calculated by only considering the uncertainty in the normalization of the TDE XLF.

3.6 Comparison with *ROSAT* Results

We check the consistency of our results with a previous study based on the *ROSAT* All-Sky Survey (RASS; Donley et al. 2002). Here, we must take into account the different TDE survey conditions between *MAXI* and *ROSAT*. Because *MAXI* is continuously monitoring the entire sky, we can derive the whole light curve of each TDE and hence its "peak" luminosity. By contrast, the detection of TDEs reported by the *ROSAT* survey was based on two snapshot observations, the one in the scanning mode during the RASS and the other in the pointing mode. Thus, in the case of *ROSAT*, it is impossible to accurately estimate the "peak" luminosity of each TDE because of the uncertainty in its peak flux time due to the scarce observations.

Table 4. Frequency of TDE occurrence at different luminosity ranges

$\log L_{\rm x}^{\rm obs}$ [1]	$\dot{N}_{p=0}$ [2]	$\dot{N}_{p=4}$ [3]
40-41	$1.2^{+1.2}_{-0.7} \times 10^{-5}$	$1.1^{+1.1}_{-0.6} \times 10^{-5}$
41-42	$4.0^{+4.0}_{-2.3} \times 10^{-6}$	$3.8^{+3.8}_{-2.2} \times 10^{-6}$
42-43	$9.0^{+9.0}_{-5.1} \times 10^{-7}$	$8.6^{+8.6}_{-4.8} \times 10^{-7}$
43-44	$1.2^{+1.2}_{-0.7} \times 10^{-7}$	$1.1^{+1.1}_{-0.6} \times 10^{-7}$
44-45	$1.1^{+1.1}_{-0.6} \times 10^{-9}$	$4.8^{+4.7}_{-2.7} \times 10^{-10}$
45-46	$1.8^{+1.8}_{-1.0} \times 10^{-10}$	$3.8^{+3.8}_{-2.2} \times 10^{-11}$
46-47	$3.1^{+3.1}_{-1.8} \times 10^{-11}$	$6.6^{+6.6}_{-3.7} \times 10^{-12}$
47-48	$2.6^{+2.5}_{-1.4} \times 10^{-12}$	$5.4^{+5.4}_{-3.1} \times 10^{-13}$

Notes.
Col. [1]: The luminosity range.
Col. [2]: The frequency of the TDE occurrence ($\rm Mpc^{-3}yr^{-1}$) in the corresponding luminosity range for $\log L_{\rm x*} = 44.6$ and $p = 0$.
Col. [3]: The same as Col. [2] but for $p = 4$.

To compare our *MAXI* results with the *ROSAT* one, we need to convert the XLF of TDEs given as a function of "peak luminosity" into an "instantaneous" XLF, which gives the probability of detecting TDEs with an instantaneous luminosity *in a single epoch*. Following Milosavljević et al. (2006), for a given instantaneous luminosity of $L'^{\rm obs}_{\rm x,ins}$, we formulate the instantaneous XLF as

$$\frac{{\rm d}\Phi'(L'^{\rm obs}_{\rm x,ins},z)}{{\rm d}\log L'^{\rm obs}_{\rm x,ins}} = \ln(10)\, L'^{\rm obs}_{\rm x,ins} \int_{\Omega=0}^{\Omega=2\pi} \frac{{\rm d}\Omega}{2\pi} \int_{L_{\rm x,min}}^{L_{\rm x,max}} {\rm d}L_{\rm x} \int_{t_{\rm p}}^{\infty} {\rm d}t \int_{M_{*,\rm min}}^{M_{*,\rm max}} {\rm d}\log M_* \times \frac{{\rm d}\Phi(L_{\rm x},z)}{{\rm d}L_{\rm x}} P(M_*) \times \Big\{ (1-f_{\rm jet})\delta_{\rm D}\Big(L'^{\rm obs}_{\rm x,ins} - L^{\rm obs}_{\rm x,ins}(C_0,L_{\rm x},t)\Big) e^{-(1+z)p(1-f_{\rm jet})\xi(L_{\rm x})t} + f_{\rm jet}\delta_{\rm D}\Big(L'^{\rm obs}_{\rm x,ins} - L^{\rm obs}_{\rm x,ins}(C_1,L_{\rm x},t)\Big) e^{-(1+z)p\ f_{\rm jet}\ \xi(L_{\rm x})t} \Big\}. \quad (18)$$

The above equation takes into account the Poisson weighted probability along the luminosity decay. The peak time $t_{\rm p}$ is chosen to be 0.1 yr, corresponding to the averaged value of our sample.

To perform this calculation, we need C_0 and C_1, the conversion factors from an intrinsic luminosity to an observed luminosity in the the *ROSAT* band (0.2–2.4 keV). Since the blackbody component can be dominant in this energy band, the term of $\omega_{\rm bb}$ in equations (3) and (4) must be estimated. We follow our assumption that the rest of the non-beamed bolometric luminosity from which the Comptonization component is subtracted is dominated by a blackbody component with a single temperature. Accordingly, we estimate the effective temperature by assuming that the emitting area of the blackbody component is $\sim \pi(3R_{\rm Sch})^2$. The color temperature is assumed to be identical to the effective one. As a result, $\omega_{\rm bb}$ is derived as a function of $L_{\rm x}$ and z. We obtain $\omega_{\rm pow} = 2.71$ for a power-law photon index of 2.0.

The predicted number of TDEs in a single epoch observation, $N_{\rm TDE}$, is calculated as

$$N_{\rm TDE} = \int_{\log L'^{\rm obs}_{\rm x,min}}^{\log L'^{\rm obs}_{\rm x,max}} \int_{z_{\rm min}}^{z_{\rm max}} \frac{{\rm d}\Phi'(L'^{\rm obs}_{\rm x,ins}, z)}{{\rm d}\log L'^{\rm obs}_{\rm x,ins}} \frac{{\rm d}V(L'^{\rm obs}_{\rm x,ins}, z)}{{\rm d}z} {\rm d}z {\rm d}\log L'^{\rm obs}_{\rm x,ins}.$$

Here, ${\rm d}V/{\rm d}z$ is the survey volume per unit redshift, which is based on the analysis by Donley et al. (2002). They detected five large-amplitude X-ray outbursts by combining the RASS and pointed *ROSAT* observations. Their survey covered $\approx 9\%$ of the sky, which is complete to the flux limit of 2×10^{-12} erg cm^{-2} s^{-1} (0.2–2.4 keV). If this flux limit is imposed, three (WPVS 007, IC 3599, and RX J1624.9+7554) out of the five TDEs are left to constitute a complete sample. We note that recently Grupe et al. (2015) have reported that the event of IC 3599 may not be a true TDE; in this case, the number of the *ROSAT* complete sample is reduced to two. In accordance with the study by Donley et al. (2002), the threshold of the observed luminosity for the identification of TDEs is set to $\log L'^{\rm obs}_{\rm x,min} = 41$.

When comparing the *ROSAT* and *MAXI* results, we should take into account the fact that the RASS performed in the soft X-ray band would easily miss obscured TDEs, unlike the case of *MAXI*. Indeed, the follow-up observations of our four TDEs with *Swift* or *XMM-Newton* indicate that two of them (*Swift* J1644+57 and NGC 4845; Burrows et al. 2011; Nikołajuk & Walter 2013) are obscured with column densities of $N_{\rm H} > 10^{22}$ cm^{-2}. From this result, we estimate the obscuration fraction to be $\sim 1/2$, and accordingly, decrease the detectable number of TDEs $N_{\rm TDE}$ by a factor of 2 to be compared with the *ROSAT* result. Also, we implicitly assume that all TDEs have hard X-ray components. Although they are not significantly required in the RASS spectra of WPVS 007 (Grupe et al. 1995) and RX J1624.9+7554 (Grupe et al. 1999), their expected contribution to the 0.5–2 keV flux can be very small ($\sim$1%) and hence cannot be well constrained with these data owing to the limited energy band and photon statistics. To confirm this assumption, future broadband observations of TDEs, like those by *eROSITA*, will be important.

We calculate $N_{\rm TDE}$ with equation (19) from our best-fit XLF models summarized in Table 3. We obtain $N_{\rm TDE}/2 = 3.2^{+3.2}_{-1.8}$ for $p = 0$ and $N_{\rm TDE}/2 = 4.0^{+3.9}_{-2.2}$ for $p = 4$, which are consistent with the observed number of TDEs (three or two) in the *ROSAT* survey. When $\lambda_{\rm Edd} = 0.1$ (corresponding to $\log L_{\rm X*} = 44.0$) is adopted instead of $\lambda_{\rm Edd} = 1.0$ ($\log L_{\rm x*} = 44.6$), the derived XLF predicts $N_{\rm TDE}/2 = 0.7^{+0.7}_{-0.4}$ for $p = 0$ and $N_{\rm TDE}/2 = 1.2^{+1.2}_{-0.7}$ for $p = 4$. These numbers are significantly smaller than three at 90% confidence level, although that for $p = 4$ is consistent with two (i.e., when the event in IC 3599 is excluded from the *ROSAT* sample). Also, under the assumption of $\lambda_{\rm Edd} = 5$ and $k_{2-10} = 70$ as a super-Eddington accretion case, the predicted TDE number is significantly higher ($N_{\rm TDE}/2 \gtrsim 4$) than the observed one regardless of the evolution index (p). Hence, we adopt $\lambda_{\rm Edd} = 1.0$ in our baseline model, which is allowed for the range of $p = 0$–4.

In the above calculations of $N_{\rm TDE}$, we have ignored possible time evolution of the X-ray spectrum of each TDE during the decay phase. According to Vasudevan & Fabian (2007), the bolometric correction factor from the 2–10 keV band (k_{2-10}) depends on Eddington ratio. Since k_{2-10} determines the relative weights between the Comptonized and blackbody components (see fourth paragraph in this Section) in our assumption, the X-ray spectrum is predicted to be time dependent. To roughly examine these effects, we calculate $N_{\rm TDE}$ by approximating that $k_{2-10} = 50$ and $k_{2-10} = 20$ when $\lambda_{\rm Edd} \geq 0.1$ and $\lambda_{\rm Edd} < 0.1$, respectively. In the case of $\lambda_{\rm Edd} = 1.0$, we obtain $N_{\rm TDE}/2 = 3.7^{+3.7}_{-2.1}$ for $p = 0$ and $N_{\rm TDE}/2 = 4.8^{+4.8}_{-2.7}$ for $p = 4$, while $N_{\rm TDE}/2 < 3$ is obtained for both $p = 0$ and 4 in the case of $\lambda_{\rm Edd} = 0.1$. Hence, the possible spectral evolution does not affect our conclusion.

3.7 Effects by Changing Fixed Parameters

In this subsection, we examine the effects on the XLF results, in particular $f_{\rm jet}$, by changing the fixed parameters in the XLF model that are difficult to be constrained from the data: (1) the Lorentz factor of the jets (Γ), (2) the dependence of the specific TDE rate on SMBH mass (λ), (3) the fraction of the intrinsic jet luminosity in $L_{\rm x}$ ($\eta_{\rm jet}$), and (4) the upper mass boundary of tidally disrupted stars ($M_{*,\rm max}$). Considering the small sample size, we perform a ML fit of the XLF by adopting an alternative value instead of the default value for each fixed parameter and check how $f_{\rm jet}$ is affected. We consider $\Gamma = 5$ and 20 (default is 10), $\lambda = -0.1$ (default is -0.4), $\eta_{\rm jet} = 0.01, 1.0$ and 10.0 (default is 0.1), and $M_{*,\rm max}/M_\odot = 10$ and 100 (default is 1). In each case, we assume the two evolution indices, $p = 0$ and $p = 4$. We regard that the minimum or maximum values considered here correspond to extreme cases within physically plausible values.

Figure 6 summarizes the constraints on $f_{\rm jet}$ plotted against Γ when one of the other parameters (λ, $\eta_{\rm jet}$, $M_{*,\rm max}$) is changed. The red and blue marks correspond to $p = 0$ and $p = 4$, respectively. If an acceptable fit is not obtained in terms of the one-dimensional KS tests (for the redshift and luminosity distributions) and/or the predicted number of TDEs in the *ROSAT* survey, we mark them in gray color. Also, when the maximum luminosity in the TDE XLF is lower than the observed ones ($\log L_{\rm X} = 47.5$), we plot the points at the position of $f_{\rm jet} = 100\%$ in gray color. These gray points should be ignored because the corresponding XLF model is rejected.

Among the acceptable parameter sets, we obtain the *maximum* upper-limit of $f_{\rm jet} = 34\%$ for $\Gamma = 20$, $\eta_{\rm jet} = 0.01$, and $p = 0$, and the *minimum* lower-limit of $f_{\rm jet} = 0.0007\%$ for

$\Gamma = 10$, $\eta_{\rm jet} = 10.0$, and $p = 4$. Thus, we conservatively estimate that the fraction of TDEs with jets among all TDEs is 0.0007–34%. This constraint is compatible with the fraction of radio loud AGNs in all AGNs ($\sim$10%). We note that $f_{\rm jet}$ depends on a combination of $\eta_{\rm jet}$ and Γ. This is mainly because the cutoff luminosity of the XLF for TDEs with jets is determined as $\eta_{\rm jet}\delta(\Gamma,\theta)^4$, with which $f_{\rm jet}$ is strongly coupled: one obtains a large value of $f_{\rm jet}$ when $\eta_{\rm jet}$ and/or Γ becomes smaller. Since Γ determines the solid-angle of the detectable relativistic jets ($\propto 1/\Gamma^2$), there is another coupling of $f_{\rm jet}$ with Γ, which partially cancels out the coupling through the cutoff luminosity.

4 Discussions

4.1 Results Summary

Utilizing a complete sample of TDEs detected in the *MAXI* extragalactic survey in the 4–10 keV band, we have, for the first time, quantitatively derived the shape of the XLF of TDEs (the occurrence rate of a TDE per unit volume) as a function of intrinsic peak luminosity at $z \lesssim 1.5$. Our XLF takes account of two TDE types, one with jets and the other without jets, and those subject to heavy absorption that would be difficult to detect in soft X-ray surveys. In the modelling of the XLF, we have taken into account the mass function of SMBHs, that of disrupted stars, the specific TDE rate as a function of SMBH mass, and relativistic beaming effects from jets, although we need to fix several parameters at reasonable values. The XLF can be converted to an "instantaneous XLF" obtained from a single-epoch observation in different energy bands, by assuming spectra of TDEs. Our baseline model, whose parameters are listed in Table 2, is found to well reproduce the number of TDEs previously detected in the *ROSAT* survey. The main finding is that the fraction of TDEs with jets among all TDEs is 0.0007–34%. Our result will serve as a reference model of a TDE XLF, which would be useful to estimate their contribution to the growth history of SMBHs and to predict TDE detections in future missions.

4.2 Comparison of TDE Rate with Previous Studies

We compare the TDE rate per unit volume based on our best-fit XLF with those estimated from previous studies. Combining the *XMM-Newton* slew survey and the RASS, Esquej et al. (2008) detected two TDEs, whose soft X-ray luminosities were $\sim 5\times10^{41}$ erg s^{-1} and $\sim 5\times10^{43}$ erg s^{-1}. They derived a TDE rate per unit volume to be $\sim 5\times10^{-6}$ Mpc^{-3} yr^{-1} for the peak luminosity of 10^{44} erg s^{-1} in the 0.2-2.0 keV band. Our result in Table 4 predicts the rate of unobscured TDEs with the peak luminosity $> 10^{41}$ erg s^{-1} (4–10 keV) to be $\sim 5\times10^{-6}$ Mpc^{-3} yr^{-1} at $z = 0$, which is in good agreement with the estimate by Esquej et al. (2008).

Maksym et al. (2010) studied a TDE in the galaxy cluster Abell 1689, using *Chandra* and *XMM-Newton*. The TDE rate "per galaxy" was estimated to be 6×10^{-5} galaxy^{-1} yr^{-1} for the minimum luminosity in the 0.3–2.5 keV band of 10^{42} erg s^{-1}. Our XLF predicts a TDE rate of $\sim 1\times10^{-4}$ galaxy^{-1} yr^{-1} for peak luminosities of $\log L_{\rm x} > 42$, by adopting the spatial density of galaxies of $\phi_0 = 0.007$ galaxy Mpc^{-3}. The discrepancy by a factor of $\sim$2 may be explained if only half number of member galaxies in Abell 1689 can produce TDEs detectable by their analysis, as mentioned in Maksym et al. (2010).

It is interesting to compare our TDE rate with that obtained from the flux-complete, optically-selected sample by van Velzen & Farrar (2014) using archival Sloan Digital Sky Survey data. They detected two TDE candidates, and estimated the TDE rate of $\sim (4-8)\times10^{-8}$ yr^{-1} Mpc^{-3} for SMBH masses of $\sim 10^7\ M_\odot$. Our estimate for the corresponding luminosity ($\log L_{\rm X} \gtrsim 43$) is $\sim 1\times10^{-7}$ yr^{-1} Mpc^{-3}. This is higher than the TDE rate of van Velzen & Farrar (2014). It may be owing to dust extinction, which reduces the number of TDE flares detectable in the optical band. Indeed, if we correct the optical TDE rate for obscuration by a factor of 2, it becomes $\sim (8-16)\times10^{-8}$ yr^{-1} Mpc^{-3}, which is consistent with the X-ray result.

4.3 Contribution of TDEs to X-ray Luminosity Functions of Active Galactic Nuclei

It is possible that the XLF of AGNs may be contaminated by TDEs, which are difficult to be distinguished from AGNs in observations of limited numbers. To investigate this effect, we calculate the instantaneous XLFs of TDEs based on our best-fit parameters with equation (18). Figure 7 plots the results in the 2–10 keV band at the low redshift ($0.002 < z < 0.2$) and high redshift ($1.0 < z < 1.2$) ranges for the two evolution indices, $p = 0$ and $p = 4$. The error region at 90% confidence level due to the uncertainty in the normalization is also indicated. The luminosity range below the sensitivity limit where the TDE XLF is not directly constrained from the *MAXI* survey is indicated by the dashed lines.

For comparison, we overplot the hard XLF of AGNs obtained by Ueda et al. (2014) at $z = 0.1$ and $z = 1.1$ for the two redshift ranges, respectively. As noticed from Figure 7, the instantaneous XLF of TDEs are far below the observed AGN XLF at $0.002 < z < 0.2$, indicating the contribution of TDEs is negligible in the local universe. At $1.0 < z < 1.2$, the TDE contribution to the AGN XLF is also negligible at high luminosities, while it could be significant at the lowest luminosity range. However, the model of the TDE XLF in this region is just an extrapolation from the result at the low redshift range, and must be constrained by more sensitive surveys to reach any conclusions.

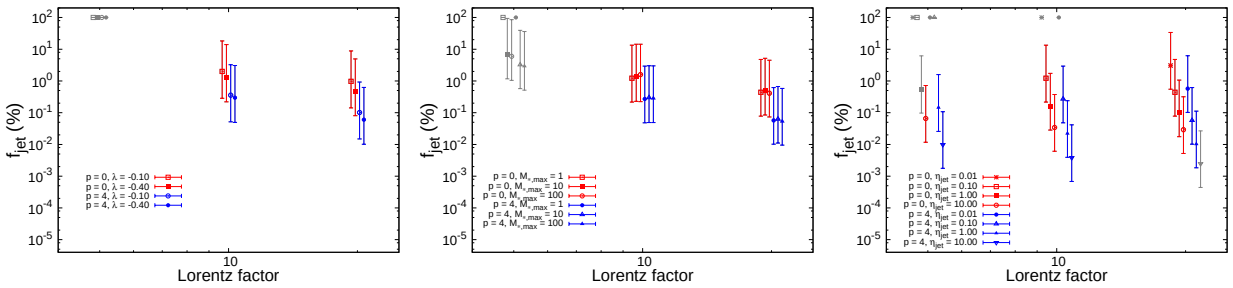
f_jet (%)
Lorentz factor
p = 0, λ = -0.10
p = 0, λ = -0.40
p = 4, λ = -0.10
p = 4, λ = -0.40
p = 0, M_*,max = 1
p = 0, M_*,max = 10
p = 0, M_*,max = 100
p = 4, M_*,max = 1
p = 4, M_*,max = 10
p = 4, M_*,max = 100
p = 0, η_jet = 0.01
p = 0, η_jet = 0.10
p = 0, η_jet = 1.00
p = 0, η_jet = 10.00
p = 4, η_jet = 0.01
p = 4, η_jet = 0.10
p = 4, η_jet = 1.00
p = 4, η_jet = 10.00

Fig. 6. The constraint on $f_{\rm jet}$ plotted against the jet Lorentz factor Γ for various choices of the other parameters in the XLF (λ, $\eta_{\rm jet}$, $M_{*,\rm max}$). For clarity, the

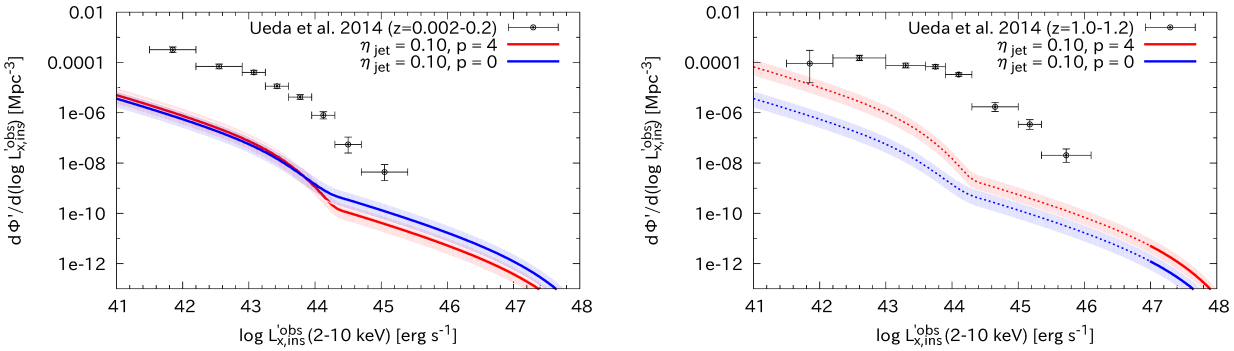

Fig. 7. Comparison of the instantaneous XLF of TDEs (our work) and the XLF of AGNs (Ueda et al. 2014) in the 2–10 keV band. The upper and lower panels show the results in the low ($z = 0.1$) and high ($z = 1.1$) redshift ranges, respectively. The 1σ Poisson errors are attached to the AGN XLF.

4.4 Mass Accretion History of SMBHs by TDEs

TDEs contribute to the growth of SMBHs as argued by Soltan (1982) for AGNs. We here calculate the evolution of the mass density of SMBHs by TDEs as done for AGNs (e.g., Marconi et al. 2004; Shankar et al. 2004). The bolometric luminosity of a TDE can be related to the mass accretion rate $\dot{M}_{\rm acc}$ via the mass-to-radiation conversion efficiency ϵ as

$$L_{\rm bol} = \epsilon c^2 \dot{M}_{\rm acc}. \tag{19}$$

The mass growth rate of the SMBH is given by

$$\dot{M}_{\rm BH} = (1-\epsilon)\dot{M}_{\rm acc}. \tag{20}$$

We formulate the SMBH mass-density equation as

$$\rho(z) = \int_{z_{\rm s}}^{z} {\rm d}z \frac{{\rm d}t}{{\rm d}z} \int_{L_{\rm x,min}}^{L_{\rm x,max}} {\rm d}L_{\rm x} \frac{{\rm d}\Phi(L_{\rm x}, z)}{{\rm d}L_{\rm x}} \int_{M_{*,\rm min}}^{M_{*,\rm max}} P(M_*) {\rm d}\log M_* \times \frac{1-\epsilon}{\epsilon c^2} \int_{t_{\rm p}}^{\infty} \{(1-f_{\rm jet})L_{\rm peak} + f_{\rm jet} L_{\rm peak}^{\rm jet}\} \left(\frac{t}{t_{\rm p}}\right)^{-5/3} {\rm d}t, \tag{21}$$

where $z_{\rm s}$, $L_{\rm peak}$, and $L_{\rm peak}^{\rm jet}$ are the initial redshift from which the calculation starts, the peak bolometric luminosity without jets, and that with jets. Here, $L_{\rm peak}$ is set to the Eddington luminosity, while $L_{\rm peak}^{\rm jet}$ is the sum of the Eddington luminosity and intrinsic jet luminosity. In equation (21), we assume that the time taken for most of the mass of a disrupted star to fall onto the SMBH is shorter than the cosmological time scale.

We adopt the mass-to-radiation conversion efficiency of $\epsilon = 0.1$ similarly to the case of AGNs. Figure 8 shows the cumulative SMBH mass-density ($M_\odot$ Mpc^{-3}) calculated from $z_{\rm s} = 1.5$. We find that the total mass density at $z = 0$ is at most $7 \times 10^2 M_\odot$ Mpc^{-3} even for the case of $p = 4$. This indicates that the SMBH mass-density contributed by TDEs is much less than that of AGNs (e.g., Ueda et al. 2014). This is what is expected from the comparison of the XLF between TDE and AGN as described in the previous subsection.

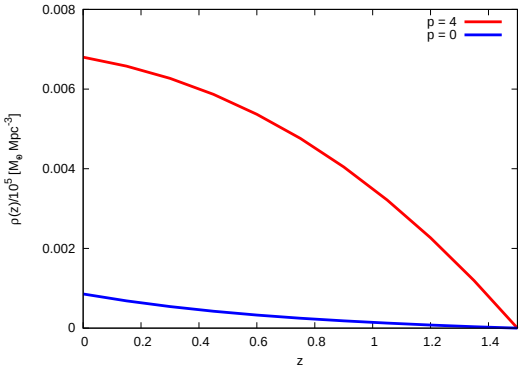

Fig. 8. The evolution of SMBH mass-density caused by TDEs. Each line is colored in accordance with the notation in the figure.

5 Summary

We have derived the XLF of TDEs, i.e., the occurrence rate of a TDE per unit volume as a function of intrinsic peak luminosity, from the *MAXI* extragalactic survey. Our sample consists of four TDEs, *Swift* J1112-82, *Swift* J1644+57, *Swift* J2058+05, and NGC 4845, detected in the first 37 months data of *MAXI*/GSC at high Galactic latitudes ($|b| > 10^\circ$). It is complete to a flux limit of $\sim 3 \times 10^{-11}$ erg s^{-1} cm^{-2} (4–10 keV), and is less affected with absorption than those detected in lower energy bands. In fact, two out of the four TDEs show significant absorptions in the X-ray spectra.

We formulate the shape of the TDE XLF, based on the mass function of SMBHs, that of tidally disrupted stars, and the specific TDE rate as a function of SMBH mass. We take account of two distinct types of TDEs, those with jets and those without them, and also the relativistic beaming from the jets. To incorporate effects of the cosmological evolution, we assume two cases where the XLF is constant over redshift or is proportional to $(1+z)^4$. ML fits are performed to the observed TDE sample, with the normalization of the XLF (i.e., TDE rate) and the fraction of TDEs with jets among all TDEs, $f_{\rm jet}$, allowed to vary. We then verify the best-fit model by checking consistency with the *ROSAT* study by Donley et al. (2002). Consequently, we find that $f_{\rm jet}$ is constrained to be 0.0007–34%, consistent with the case of AGNs.

On the basis of our best-fit TDE XLF, we have estimated the contribution of TDEs to instantaneous XLFs of AGNs and to the evolution of the SMBH mass density. It is found to be much smaller than those of AGNs, indicating that the effect by TDEs to the growth of SMBHs is negligible at $z \lesssim 1.5$. Future observations of TDEs, including the *eROSITA* survey, will enable us to establish more accurate statistical properties of TDEs over wide luminosity and redshift ranges.

Part of this work was financially supported by the Grant-in-Aid for JSPS Fellows for young researchers (TK) and for Scientific Research 26400228 (YU). This research has made use of *MAXI* data provided by RIKEN, JAXA and the *MAXI* team.

Appendix A Detection of X-ray Transient Events from *MAXI* Data

This section describes the image analysis of the *MAXI*/GSC data employed to extract the transient X-ray events. The method is essentially the same as that of Hiroi et al. (2013) used to produce the 37-month catalog, but is applied to 37 (or 12) individual images binned in 30 days (or 90 days) to obtain the light curves of all sources including newly detected transient objects.

The entire all-sky image in each time bin is divided into 768 areas of $14^\circ \times 14^\circ$ size centered at the coordinates defined in the HEALPix software (Górski et al. 2005). Circular regions around the very bright sources Sco X-1, Cyg X-2, and Crab Nebula are not used in our analysis to avoid systematic errors in the calibration of the point spread function (PSF). First, combining the observed image and the model of the background (the cosmic X-ray background plus the non X-ray background), we make the significance map; an example is shown in Figure 1. Here the significance at each position is simply calculated as the background-subtracted counts divided by the square root of total counts in the $0^\circ.1 \times 0^\circ.1$ region around it. Then, excess points with the peak significance above 5.5σ are left as source candidates. We regard those whose positions do not match any sources in the 37-month *MAXI*/GSC catalog within 1° as candidates of transient sources newly detected in this time-sliced image analysis.

To determine the fluxes of all source candidates, we then perform image fitting by a model composed of the background and PSFs. Here we consider PSFs of all sources in the 37-month *MAXI* catalog and those of the transient candidates extracted above. The PSFs are calculated with the *MAXI* simulator (Eguchi et al. 2009) by assuming the spectrum of the Crab nebula. The fluxes of all sources (in units of Crab) and the normalization of the background are left as free parameters. The positions of the 37-month *MAXI* catalog sources are fixed according to the results by Hiroi et al. (2013), while those of the transient candidates are set to be free parameters. To find the best-fit parameters and their statistical errors, we employ the maximum likelihood algorithm based on the C statistics (Cash 1979), utilizing the MINUIT software package. To ensure complete detections of transient events, we repeat the above procedures twice for each image. Namely, we again make the significance map based on the best-fit model including the PSFs, search for remaining residuals with the significance above 5.5σ, and then perform the image fitting by including new source candidates.

As the results, we detect 10 transient events in total at high galactic latitudes ($|b| > 10^\circ$), whose detection significance exceeds 5.5 in either of the analyzed images. Here we have paid careful attention to exclude fake events caused by the Sun light contamination by checking the image and spectra. Table A summarizes the basic information of the events. The parameters are derived from an image where the event was detected with the highest detection significance among all time bins.

To find possible counterparts of our transient events, we check major X-ray source catalogs and the literature regarding Gamma-ray Bursts and TDEs covering our observation epoch: Palermo *Swift* BAT X-ray catalog (Cusumano et al. 2010), *Fermi* 2$^{\rm nd}$ LAT Catalog (Nolan et al. 2012), *ROSAT* Bright Source Catalog (Voges et al. 1999), *Swift* BAT 70-month Catalog (Baumgartner et al. 2013), *Swift* Transient Monitor Catalog (Krimm et al. 2013), First *XMM-Newton* Sky Slew Survey Catalog (Saxton et al. 2008), *INTEGRAL* General

Reference Catalog (version 36), and papers by Cenko et al. (2012), Zauderer et al. (2013), Serino et al. (2014), and Brown et al. (2015). We identify the counterpart if its position is within the 3σ positional error (corresponding to 99% confidence level) of a *MAXI* transient source. The error consists of the statistical one and systematic one, $\sigma_{\rm pos} = (\sigma_{\rm stat}^2 + \sigma_{\rm sys}^2)^{1/2}$. Here, the systematic error is chosen to be $0^\circ.05$ according to the previous studies (Hiroi et al. 2011; Hiroi et al. 2013). Figure 1 plots the 10-days bin light curves in the 3–10 keV band of all transient events other than the three TDEs (*Swift* J1112-82, *Swift* J1644+57, and *Swift* J2058+05).

Table A. Information of Transient Events

MAXI Name	R.A.	Decl.	$\sigma_{\rm pos}$	$s_{\rm D}$	$f_{4-10{\rm keV}}$	Hardness ratio	Flare Time	Counterpart	Type
[1]	[2]	[3]	[4]	[5]	[6]	[7]	[8]	[9]	[10]
2MAXIt J0745−504	116.451	-50.496	0.216	6.07	5.16	> 0.87	55727–55756	HD 63008	Star
2MAXIt J1108−829	167.064	-82.914	0.191	6.70	2.88	0.19 ± 0.14	55727–55756	*Swift* J1112.2-8238	Tidal Disruption Event
2MAXIt J1159+238	179.814	23.876	0.185	5.77	2.66	> 0.71	55877–55906		
2MAXIt J1507−217	226.882	-21.743	0.122	10.35	8.59	0.33 ± 0.11	55127–55156	GRB 091120	Gamma-Ray Burst
2MAXIt J1517+067	229.350	6.793	0.198	5.79	1.79	0.23 ± 0.18	55637–55726		
2MAXIt J1645+576	251.379	57.604	0.131	8.83	3.18	0.18 ± 0.12	55637–55726	*Swift* J164449.3+573451	Tidal Disruption Event
2MAXIt J1807+132	271.806	13.269	0.184	5.68	2.73	0.28 ± 0.18	55697–55726		
2MAXIt J1944+022	296.170	2.203	0.219	6.12	2.45	< 0.32	55997–56086	*Swift* J1943.4+0228	CV
2MAXIt J2058+053	314.578	5.377	0.202	6.39	3.39	0.19 ± 0.15	55697–55726	*Swift* J2058.4+0516	Tidal Disruption Event
2MAXIt J2313+030	348.455	3.037	0.223	6.01	4.09	< 0.23	55097–55126	SZ Psc	RSCVn

Notes.
Col. [1]: *MAXI* Name.
Col. [2]: Right ascension in units of degree.
Col. [3]: Declination in units of degree.
Col. [4]: 1σ statistical position error.
Col. [5]: Detection Significance.
Col. [6]: Average flux over a time interval in the 4-10 keV band in units of mCrab.
Col. [7]: Hardness ratio and its 1σ error.
Col. [8]: Duration of 30-days bin used when the source is detected.
Col. [9]: Name of the counterpart.
Col. [10]: Type of the counterpart.

Appendix B *MAXI* Results for TDE Candidates Suggested in the *Swift*/BAT Data

We check if *MAXI* also found any signals of the TDE candidates reported by Hryniewicz & Walter (2016), who used the *Swift*/BAT ultra-hard X-ray (20–195 keV) data taken between 2005 and 2013. The number of TDE candidates detected within the 37-month period of our *MAXI* data is four. We confirm that all of them are not significantly detected in the 4–10 keV image integrated over a 30 day period covering the flare time. Thus, it is justified not to include these events in our analysis. Table B summarizes the 5.5σ upper limit of the fluxes in the 4–10 keV band together with the basic information for each TDE. We find that in all events the *MAXI* upper limit is smaller by a factor of $\sim$4 than that expected from the averaged BAT flux in the same epoch by assuming a photon index of 2. The reason is unclear, but these events might be subject to heavy (nearly Compton thick) obscuration.

References

Aharon, D., Mastrobuono Battisti, A., & Perets, H. B. 2015, arXiv:1507.08287

Arcavi, I., Gal-Yam, A., Sullivan, M., et al. 2014, ApJ, 793, 38

Bade, N., Komossa, S., & Dahlem, M. 1996, A&A, 309, L35

Baumgartner, W. H., Tueller, J., Markwardt, C. B., et al. 2013, ApJS, 207, 19

Blanton, M. R., Dalcanton, J., Eisenstein, D., et al. 2001, AJ, 121, 2358

Brown, G. C., Levan, A. J., Stanway, E. R., et al. 2015, MNRAS, 452, 4297

Burrows, D. N., Kennea, J. A., Ghisellini, G., et al. 2011, Nature, 476, 421

Cash, W. 1979, ApJ, 228, 939

Cenko, S. B., Krimm, H. A., Horesh, A., et al. 2012, ApJ, 753, 77

Chabrier, G. 2003, PASP, 115, 763

Cusumano, G., La Parola, V., Segreto, A., et al. 2010, A&A, 524, A64

Donley, J. L., Brandt, W. N., Eracleous, M., & Boller, T. 2002, AJ, 124, 1308

Eguchi, S., Hiroi, K., Ueda, Y., et al. 2009, Astrophysics with All-Sky X-Ray Observations, 44

Esquej, P., Saxton, R. D., Freyberg, M. J., et al. 2007, A&A, 462, L49

Esquej, P., Saxton, R. D., Komossa, S., et al. 2008, A&A, 489, 543

Evans, C. R., & Kochanek, C. S. 1989, ApJL, 346, L13

Ferrarese, L. 2002, Current High-Energy Emission Around Black Holes, 3

Gehrels, N. 1986, ApJ, 303, 336

Gezari, S., Martin, D. C., Milliard, B., et al. 2006, ApJL, 653, L25

Gezari, S., Basa, S., Martin, D. C., et al. 2008, ApJ, 676, 944

Gezari, S., Chornock, R., Rest, A., et al. 2012, Nature, 485, 217

Górski, K. M., Hivon, E., Banday, A. J., et al. 2005, ApJ, 622, 759

Grupe, D., Beuerman, K., Mannheim, K., et al. 1995, A&A, 300, L21

Grupe, D., Thomas, H.-C., & Leighly, K. M. 1999, A&A, 350, L31

Grupe, D., Komossa, S., & Saxton, R. 2015, ApJL, 803, L28

Guillochon, J., & Ramirez-Ruiz, E. 2013, ApJ, 767, 25

Hiroi, K., Ueda, Y., Isobe, N., et al. 2011, PASJ, 63, 677

Hiroi, K., Ueda, Y., Hayashida, M., et al. 2013, ApJS, 207, 36

Holoien, T. W.-S., Prieto, J. L., Bersier, D., et al. 2014, MNRAS, 445, 3263

Hryniewicz, K., & Walter, R. 2016, A&A, 586, A9

Irwin, J. A., Henriksen, R. N., Krause, M., et al. 2015, ApJ, 809, 172

Isobe, N., Sato, R., Ueda, Y., et al. 2015, ApJ, 798, 27

Kippenhahn, R., & Weigert, A. 1990, Stellar Structure and Evolution, XVI, 468 pp. 192 figs.. Springer-Verlag Berlin Heidelberg New York. Also Astronomy and Astrophysics Library,

Komossa, S., & Bade, N. 1999, A&A, 343, 775

Komossa, S. 2012, European Physical Journal Web of Conferences, 39, 2001

Krimm, H. A., Holland, S. T., Corbet, R. H. D., et al. 2013, ApJS, 209, 14

Kroupa, P. 2001, MNRAS, 322, 231

Li, L.-X., Narayan, R., & Menou, K. 2002, ApJ, 576, 753

Magorrian, J., & Tremaine, S. 1999, MNRAS, 309, 447

Maksym, W. P., Ulmer, M. P., & Eracleous, M. 2010, ApJ, 722, 1035

Marconi, A., & Hunt, L. K. 2003, ApJL, 589, L21

Marconi, A., Risaliti, G., Gilli, R., et al. 2004, MNRAS, 351, 169

Matsuoka, M., Kawasaki, K., Ueno, S., et al. 2009, PASJ, 61, 999

Mihara, T., Nakajima, M., Sugizaki, M., et al. 2011, PASJ, 63, 623

Milosavljević, M., Merritt, D., & Ho, L. C. 2006, ApJ, 652, 120

Miyaji, T., Hasinger, G., & Schmidt, M. 2001, A&A, 369, 49

Negoro, H., Ozawa, H., Suwa, F., et al. 2012, Astronomical Data Analysis Software and Systems XXI, 461, 797

Nikołajuk, M., & Walter, R. 2013, A&A, 552, A75

Nolan, P. L., Abdo, A. A., Ackermann, M., et al. 2012, ApJS, 199, 31

Pasham, D. R., Cenko, S. B., Levan, A. J., et al. 2015, ApJ, 805, 68

Pérez-González, P. G., Rieke, G. H., Egami, E., et al. 2005, ApJ, 630, 82

Phinney, E. S. 1989, The Center of the Galaxy, 136, 543

Press, W. H., Teukolsky, S. A., Vetterling, W. T., & Flannery, B. P. 1992, Cambridge: University Press, —c1992, 2nd ed.,

Rees, M. J. 1988, Nature, 333, 523

Salpeter, E. E. 1955, ApJ, 121, 161

Saxton, R. D., Read, A. M., Esquej, P., et al. 2008, A&A, 480, 611

Saxton, R. D., Read, A. M., Esquej, P., et al. 2012, A&A, 541, A106

Serino, M., Sakamoto, T., Kawai, N., et al. 2014, arXiv:1406.3912

Shankar, F., Salucci, P., Granato, G. L., De Zotti, G., & Danese, L. 2004, MNRAS, 354, 1020

Soltan, A. 1982, MNRAS, 200, 115

Stone, N., & Loeb, A. 2012, Physical Review Letters, 108, 061302

Stone, N. C., & Metzger, B. D. 2014, arXiv:1410.7772

Sugizaki, M., Mihara, T., Serino, M., et al. 2011, PASJ, 63, 635

Tomida, H., Tsunemi, H., Kimura, M., et al. 2011, PASJ, 63, 397

Ueda, Y., Akiyama, M., Hasinger, G., Miyaji, T., & Watson, M. G. 2014, ApJ, 786, 104

Ulmer, A. 1999, ApJ, 514, 180

van Velzen, S., Farrar, G. R., Gezari, S., et al. 2011, ApJ, 741, 73

van Velzen, S., & Farrar, G. R. 2014, ApJ, 792, 53

Vasudevan, R. V., & Fabian, A. C. 2007, MNRAS, 381, 1235

Voges, W., Aschenbach, B., Boller, T., et al. 1999, A&A, 349, 389

Wang, J., & Merritt, D. 2004, ApJ, 600, 149

Zauderer, B. A., Berger, E., Soderberg, A. M., et al. 2011, Nature, 476, 425

Zauderer, B. A., Berger, E., Margutti, R., et al. 2013, ApJ, 767, 152

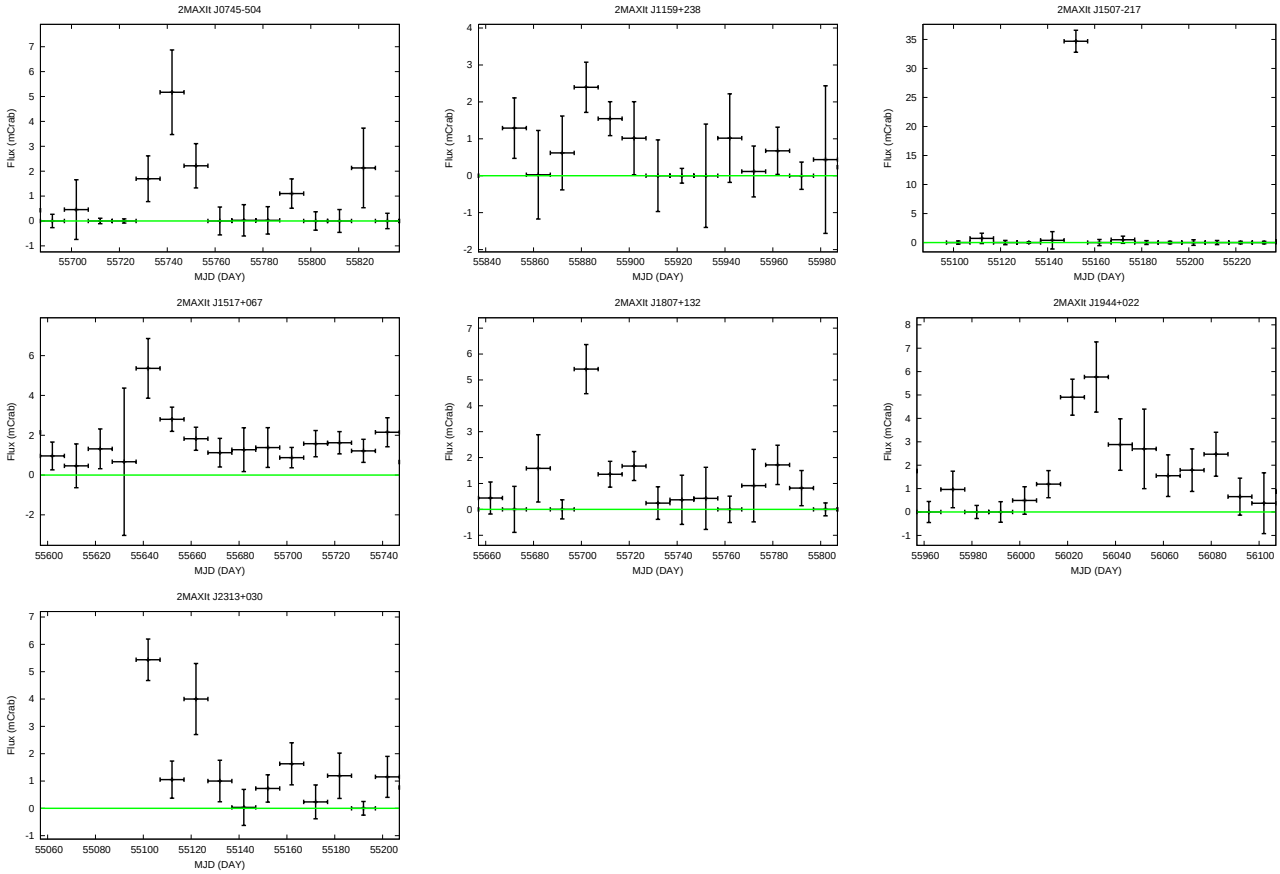

Fig. 1. The 10-days bin *MAXI* light curves in the 3–10 keV band of transient sources other than the four TDEs.

Table B. Information of *Swift*/BAT TDE Candidates

Name	R.A.	Decl.	$\hat{f}_{4-10\mathrm{keV}}$	Epoch
[1]	[2]	[3]	[4]	[5]
PGC 015259	67.341	-4.760	< 1.7	55217–55246
UGC 03317	83.406	73.726	< 1.1	55457–55486
PGC 1185375	225.960	1.127	< 3.5	55247–55276
PGC 1190358	226.370	1.293	< 3.2	55247–55276

Notes.
Col. [1]: Name of TDE candidates detected with *Swift*/BAT (Hryniewicz & Walter 2016).
Col. [2]: Right ascension in units of degree.
Col. [3]: Declination in units of degree.
Col. [4]: 5.5σ upper limit of the averaged 4–10 keV flux in a 30 day period covering the flare time, in units of mCrab.
Col. [5]: Epoch (MJD) when the upper flux limit is estimated.